

## ARTICLE OPEN



# Observation of stress corrosion cracking using real-time in situ high-speed atomic force microscopy and correlative techniques

S. Moore<sup>1</sup>✉, R. Burrows<sup>2</sup>, D. Kumar<sup>1</sup>, M. B. Kloucek<sup>1</sup>, A. D. Warren<sup>1</sup>, P. E. J. Flewitt<sup>1</sup>, L. Picco<sup>3,4</sup>, O. D. Payton<sup>1,3</sup> and T. L. Martin<sup>1</sup>

Contact-mode high-speed atomic force microscopy (HS-AFM) has been utilised to measure in situ stress corrosion cracking (SCC) with nanometre resolution on AISI Type 304 stainless steel in an aggressive salt solution. SCC is an important failure mode in many metal systems but has a complicated mechanism that makes failure difficult to predict. Prior to the in situ experiments, the contributions of microstructure, environment and stress to SCC were independently studied using HS-AFM. During SCC measurements, uplift of grain boundaries before cracking was observed, indicating a subsurface contribution to the cracking mechanism. Focussed ion beam milling revealed a network of intergranular cracks below the surface lined with a thin oxide, indicating that the SCC process is dominated by local stress at oxide-weakened boundaries. Subsequent analysis by atom probe tomography of a crack tip showed a layered oxide composition at the surface of the crack walls. Oxide formation is posited to be mechanistically linked to grain boundary uplift. This study shows how in situ HS-AFM observations in combination with complementary techniques can give important insights into the mechanisms of SCC.

*npj Materials Degradation* (2021)5:3; <https://doi.org/10.1038/s41529-020-00149-y>

## INTRODUCTION

Conjoint corrosion and stressing of a metal or alloy can result in the development of cracks which propagate through the material, causing failure due to the reduced fracture resistance<sup>1,2</sup>. This phenomenon is known as stress corrosion cracking (SCC). Forms of localised corrosion, such as SCC, can occur without any obvious outward signs of damage accumulation, whilst causing significant deterioration of component structural integrity<sup>1</sup>. Furthermore, subtle changes in environment can lead to considerable differences in SCC behaviour, resulting in its occurrence being difficult to predict. As a result, SCC is often undetected, giving rise to sudden and unexpected failure. This has resulted in a significant number of failure events across numerous structural engineering applications in a range of industries including gas, oil, and nuclear<sup>3–5</sup>.

The unpredictable nature of SCC calls for considerable research into the associated mechanisms. Techniques in which SCC processes can be imaged non-destructively and in situ are of particular importance for understanding the physical mechanisms, and the sequence in which they occur. A plethora of techniques have been implemented in previous studies. These include surface and volume measurements such as optical microscopy, electron microscopy techniques and atom probe tomography (APT), and reaction sensing techniques such as electrochemical noise and scanning vibrating electrode technique<sup>6–11</sup>. These techniques operate over a range of length- and time-scales; however, techniques that offer the highest resolution seldom facilitate the conditions necessary for in situ measurements. The work presented here uses a newly developed contact-mode high-speed atomic force microscope (HS-AFM) to obtain the high temporal and spatial resolution necessary for such measurements.

An atomic force microscope (AFM) builds topographic maps of a surface by measuring the mechanical response of a sharp probe

as it moves across a sample. AFM was invented by Binnig, Quate, and Gerber in 1986<sup>12</sup> and has since revolutionised the field of nanoscience, enabling surface characterisation with exceptional resolution in a range of environments<sup>13</sup>. However, it is limited by slow collection times. Previous experiments have been conducted using conventional AFM to measure crack propagation<sup>14–16</sup>; however, with the limited imaging rate capabilities a vast amount of information is lost. HS-AFM operates at speeds orders of magnitude faster than conventional AFMs and is capable of high-resolution imaging of structures and the measurement of mechanical properties<sup>17</sup>. HS-AFM captures multiple frames per second with nanometre-scale lateral resolution and atomic height resolution, allowing for dynamic events to be observed directly in real-time<sup>13,17,18</sup>. Furthermore, this technique is able to image in gaseous, liquid or near-vacuum environments<sup>17</sup>, making it a valuable tool for studying solid–liquid interfaces, such as for in situ corrosion studies<sup>19–21</sup>.

In this study, SCC was induced by deforming a sample of thermally sensitised American Iron and Steel Institute (AISI) Type 304 austenitic stainless steel in a solution containing 395 mg L<sup>-1</sup> aqueous sodium thiosulfate. This is a model system that can reliably and predictably produce SCC allowing for in situ measurements. Thiosulfate containing solutions are used across numerous industries including nuclear, chemical, medical, paper, etc., and are known to induce intergranular SCC (IGSCC) within sensitised austenitic stainless steels when under a tensile stress<sup>22–32</sup>. A number of previous studies have been performed analysing the IGSCC behaviour of stainless steels within thiosulfate solutions, largely conducted by reaction sensing techniques<sup>22–27,30,32</sup>. To the authors best knowledge, prior to the present study, visualisation of the mechanisms occurring had been performed using only optical microscopy or post-corrosion SEM analysis. The study presented here aims to provide dynamic, in situ observations of the cracking

<sup>1</sup>Interface Analysis Centre, HH Wills Physics Laboratory, University of Bristol, Bristol BS8 1TL, UK. <sup>2</sup>National Nuclear Laboratory, Building 102B, Stonehouse Park, Sperry Way, Stonehouse, Gloucestershire GL10 3UT, UK. <sup>3</sup>Bristol Nano Dynamics Ltd., Bristol, UK. <sup>4</sup>Department of Physics, Virginia Commonwealth University, Virginia, USA. ✉email: stacy.moore@bristol.ac.uk

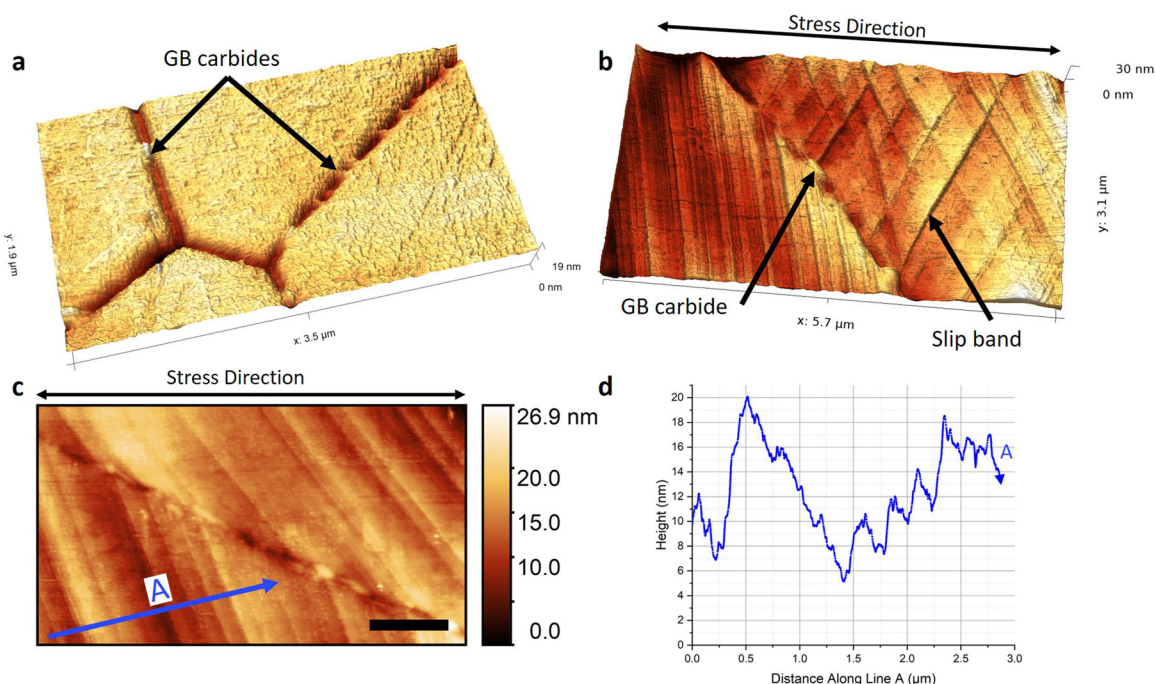


**Fig. 1** Ex situ HS-AFM measurements of sensitisation and strain. Images show 3D HS-AFM topographic maps of: **a** GBs and GB carbide precipitates within thermally sensitised AISI Type 304 stainless steel, and **(b)** slip bands in sensitised AISI Type 304 stainless steel across a GB. Also shown is: **c** an HS-AFM topographic map of slip bands in sensitised AISI Type 304 stainless steel across a GB (scale bar: 1 μm), and **(d)** a line profile along the line labelled A shown in **(c)** as a dark blue line, showing variation in height across dislocation steps. Height measurements have an error of  $\pm 15$  pm. Additional topographic images showing measurements of strain are given in Supplementary Fig. 2.

process as well as high-resolution topographical, subsurface and chemical ex situ analysis.

Crack initiation and propagation mechanisms are yet to be conclusively identified. The current literature regarding sensitised Type 304 stainless steel in thiosulfate containing solutions may be coarsely summarised into two main theories: film rupture and anodic dissolution<sup>22,27,29,30</sup>, and hydrogen induced fracture<sup>25,26,30</sup>. High crack velocities of up to  $8 \mu\text{m s}^{-1}$  have been observed in this system that could not be explained by a dissolution model alone<sup>22</sup>. Anodic dissolution was proposed by Newman et al. who also theorised that the crack velocity was increased by fracture of strain-induced martensite at the grain boundaries (GBs) ahead of the crack tip<sup>22</sup>. However, the posited effects of strain-induced martensite on crack velocity differ<sup>22,24,27</sup>. Hydrogen induced fracture has been suggested within other works to explain brittle microcracks occurring along multiple GBs<sup>25,26,30</sup>. Despite conflicting models, there is a consensus that elemental sulfur at the crack tip is key within this SCC system. Adsorbed sulfur prevents repassivation by enhancing dissolution of Fe and Ni at sensitised GBs<sup>22,24,30</sup> and/or acting as a catalyst to hydrogen entry into the matrix ahead of the crack tip possibly resulting in embrittlement<sup>25,26,30</sup>.

Within the work presented here, the HS-AFM technique was applied with the aim of better understanding the underlying mechanisms occurring within this IGSCC system. IGSCC is the result of a combination of three factors: susceptible microstructure, environment, and local tensile stress<sup>11</sup>. Within the first part of this study, these three factors were studied separately to deconvolute their individual contributions to IGSCC. It is well recognised that these factors act synergistically and that their behaviours will differ when isolated, this in itself being a strong driver for in situ studies where all factors are acting simultaneously. In the second part of the study the three factors are brought together to initiate and study IGSCC. In addition to HS-AFM analysis, complementary measurements of crack tip chemistry are performed by APT and energy dispersive X-ray

spectroscopy (EDX), and subsurface cracking is evaluated by focussed ion beam (FIB) and scanning electron microscopy (SEM). This combination allowed for a more complete characterisation of the IGSCC phenomenon.

## RESULTS AND DISCUSSION

Measurements of individual factors leading to SCC

Figure 1a shows a 3D HS-AFM topographic map collected from a sample of AISI Type 304 stainless steel heat treated at 600 °C for 70 h to produce a thermally sensitised microstructure<sup>33</sup>. The material and sensitisation conditions were selected to produce material that may act as a proxy to specific nuclear applications<sup>33</sup>, whilst also being relevant within other industries. The microstructure of this material was measured by electron backscattered diffraction (EBSD) as shown in Supplementary Fig. 1. The grain size varied from approximately 1 to 43 μm, with an average diameter of 15 μm and a standard deviation of 9 μm. The image in Fig. 1a contains two triple points where three GBs meet. Present within these GBs are 30–300 nm diameter precipitates. Based on previous works for AISI Type 304 stainless steel heat treated at 700 °C<sup>33,34</sup>, these precipitates are presumed to be chromium rich carbides (predominantly  $M_{23}C_6$ , where M is principally Cr). The precipitation of these carbides is known to result in the depletion of Cr adjacent to the GB increasing its susceptibility to IGSCC<sup>1</sup>. These precipitates are harder than the matrix, and as such topographic contrast is generated during polishing, they are also electrochemically noble and so would resist any dissolution in the colloidal silica solution. In contrast, the GBs are preferentially etched during sample preparation and so appear topographically lower.

To isolate the effects of stress in the absence of corrosion, a test specimen was deflected in a three-point strain rig before imaging. A more detailed description of the set-up is given in the Methods section. HS-AFM measurements were collected along the apex of the bend, in areas of maximum stress, shown in Fig. 1b, c. AISI

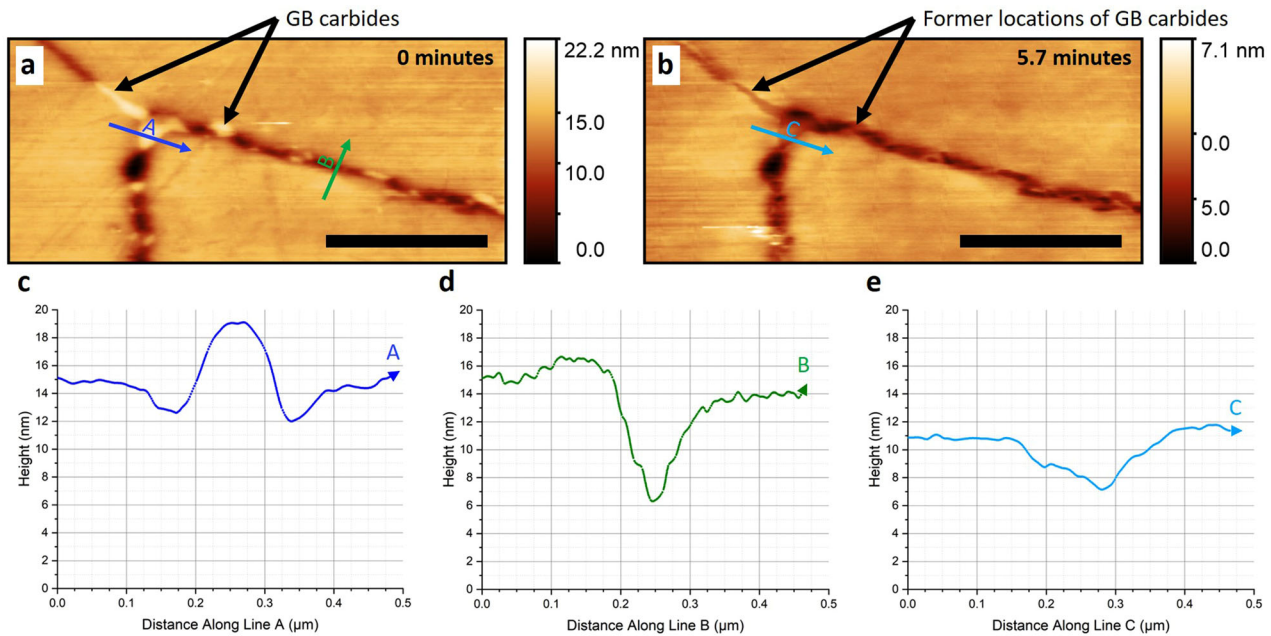


**Fig. 2** In situ HS-AFM measurements of localised corrosion. Images show HS-AFM topographic maps from a time-lapse of thermally sensitised AISI Type 304 stainless steel undergoing corrosion within  $395 \text{ mg L}^{-1}$  aqueous sodium thiosulfate at: **a** 0 min (scale bar:  $1 \mu\text{m}$ ), and **(b)** 5.7 min (scale bar:  $1 \mu\text{m}$ ). Each topographic image was collected over 0.5 s. Also shown are line profiles of height changes collected across: **(c)** Line A indicated in **(a)** as a dark blue line, **d** Line B indicated in **(a)** as a green line, **e** Line C indicated in **(b)** as a light blue line. Height measurements have an error of  $\pm 15 \text{ pm}$ .

Type 304 stainless steel is austenitic and so has a face centred cubic (FCC) crystallographic structure which, when stressed, produces slip on the most closely packed  $\{111\}$  planes<sup>35,36</sup>. Figure 1b shows slip bands forming at regular intervals, with differing directions in each grain either side of the GB; as each grain has a different crystallographic orientation. This phenomenon has been observed within other AFM studies of deformed austenitic stainless steels<sup>35–37</sup>. In some areas, the slip bands have two directions within a single grain, due to the activation of a second slip system, indicative of higher levels of strain, or a slip direction with a similar Schmid factor<sup>35,37</sup>. A line profile showing height changes across slip bands is shown in Fig. 1d. Single dislocations within this material are known to have a magnitude of  $2.58 \times 10^{-10} \text{ m}$ , i.e. the magnitude of one Burgers vector<sup>38</sup>. Steps with height changes down to approximately  $5 \times 10^{-10} \text{ m}$  were observed, corresponding to two slip dislocations. Larger height changes are also seen, corresponding to the movement of multiple dislocations, owing to the high level of local strain induced in the sample.

Next, a specimen was imaged under  $395 \text{ mg L}^{-1}$  aqueous sodium thiosulfate, in the absence of applied stress. Figure 2a, b shows the same region before and after 5.7 min of continuous monitoring within the corrosive thiosulfate solution, respectively. Preferential dissolution of features identified as carbide precipitates is evident. Intergranular micro-pits are located at the previous locations of carbide precipitates. Line profiles collected before corrosion took place show the height profile of the GB with and without a carbide precipitate, Fig. 2c and d, respectively. Figure 2e shows that GB precipitate height was significantly reduced, though not removed completely.

The gradual reduction of carbide precipitate size and the final line scan collected (Fig. 2e) suggests that carbide precipitate dissolution may have occurred. However, dissolution of the carbide precipitates is not expected since they are typically more noble with respect to the bulk. As such it may be argued that the regions adjacent to the carbide precipitates corroded resulting in

the carbide being lost, as observed in some works for chloride-containing solutions<sup>19</sup>.

Studies of thermally sensitised Type 304 stainless steel in thiosulfate solutions without applied stress have been performed in other works with varying reports<sup>26,31</sup>. Some studies found that thiosulfate does not result in anodic activity or localised corrosion in the absence of stress<sup>22–24,31</sup>. However, in other works thiosulfate was found to initiate and propagate localised corrosion processes in such a way that the role of stress was considered to be secondary<sup>26</sup>. However, these experiments were performed by reaction sensing techniques and precise reaction sites were not reported. The observations made in this study show that thiosulfate does indeed have a corrosive effect on the sample surface, and this occurs at the GB carbide precipitates positioned on sensitised GBs. This dissolution process may occur at the crack tip during IGSCC, resulting in stress accumulation at the resultant micro-pits. However, this process may not occur during IGSCC due to the synergistic nature of the individual factors.

An additional factor to consider within these measurements is that the HS-AFM probe mechanically interacts with the surface of the sample, and so may affect the rate at which corrosion occurs, such as by causing a local stirring effect. This must be noted when considering the timescales of observed reactions. The effect of the probe on mass transfer has been explored in other works. In a study by Burt et al. it was found that cantilever beams similar to those used within the presented study hindered diffusion processes<sup>39</sup>. This may result in the build-up of an aggressive solution and so promotion of corrosion processes, as observed. When the same material was imaged within non-corrosive conditions, such as within deionised water, no such reactions are observed. It can be concluded, therefore, that these observations are not a result of the action of the tip alone.

#### In situ HS-AFM measurements of SCC

By combining the factors studied individually, IGSCC was induced within a sample allowing for in situ and ex situ IGSCC studies. IGSCC was initiated in a sample of thermally sensitised AISI Type

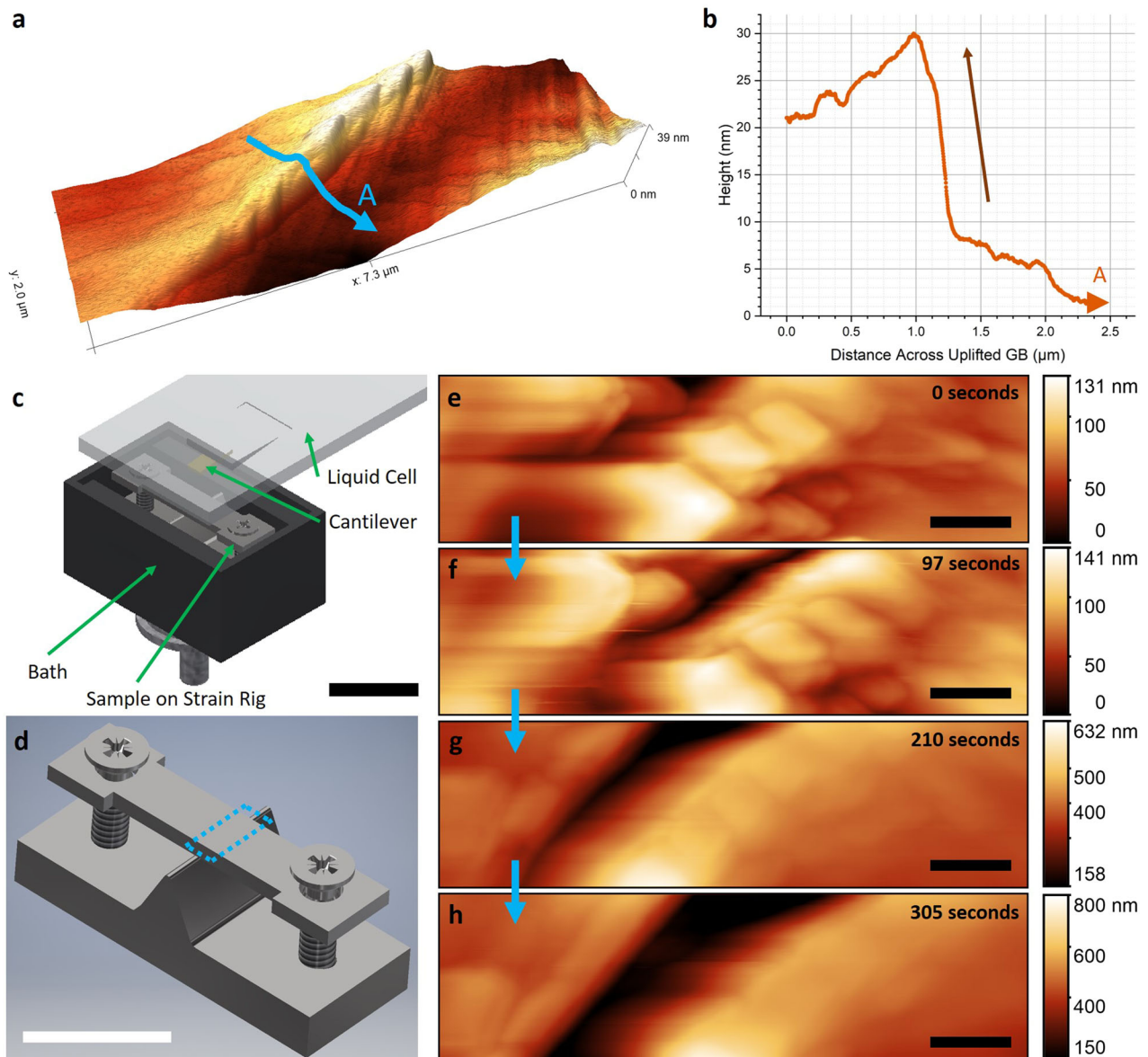


**Fig. 3** In situ HS-AFM measurements of IGSCC. **a** An HS-AFM topographic map showing uplifting of a GB prior to IGSCC occurring, and **(b)** a height profile collected along the line labelled A shown in **(a)** as a light blue line demonstrating the uplift effect. Height measurements have an error of  $\pm 15$  pm. Schematic images are also shown, **(c)** of the labelled HS-AFM SCC set-up (scale bar: 1 cm), and **(d)** of the three-point strain rig design with the area imaged outlined with a dotted blue box (scale bar: 1 cm), created using Autodesk Inventor 2019. Also, sequential HS-AFM topographic maps showing a crack propagation as IGSCC occurs at: **(e)** 0 s (scale bar: 1  $\mu\text{m}$ ), **(f)** 97 s (scale bar: 1  $\mu\text{m}$ ), **(g)** 210 s (scale bar: 1  $\mu\text{m}$ ), **(h)** 305 s (scale bar: 1  $\mu\text{m}$ ). Each topographic map was collected at a frame rate of  $2 \text{ s}^{-1}$ . Additional images showing the set-up are given in Supplementary Fig. 3.

304 stainless steel whilst being monitored by HS-AFM by stressing to a threshold following a period of unstressed immersion. This period was optimised such that time to SCC initiation was minimised, as described in the Methods section. Pre-exposure to the solution is postulated to result in oxidation of a small number of GBs, these act as initiation points upon the application of tensile stress. Areas undergoing cracking were identified using the HS-AFM's optical microscope and measurements were performed ahead of the crack tip, Fig. 3a. This image was collected approximately 40 min following the onset of cracking. Figure 3a shows two grains separated by a GB, the grain to the right of the GB contains slip bands arising from two slip systems. The grain to the left of the GB contains single slip and is uplifted at the GB compared with the grain on the right, as emphasised by the line profile shown in **(b)**. Other instances of GB uplift have been

observed under similar circumstances (Supplementary Fig. 4). These occurrences are located just ahead of the visible crack tip.

Uplifted GBs are topographically raised by 10 s of nanometres compared to stressed GBs (Fig. 1b and Supplementary Fig. 2), indicating that this phenomenon is not solely due to the effects of sample deformation. The uplift effect occurs ahead of the crack tip and was not observed elsewhere on the surface. Hence it is an effect local to the crack tip. To the best of author's knowledge GB uplift has not been reported in other works. The highest features present along the GB in Fig. 3a may be identified as carbide precipitates, slip bands, or an oxide layer distributed along the GB. It is likely that GB uplift is the result of concentrated strain ahead of the crack tip in combination with local corrosion processes. Subsurface processes must also be considered. This may result in

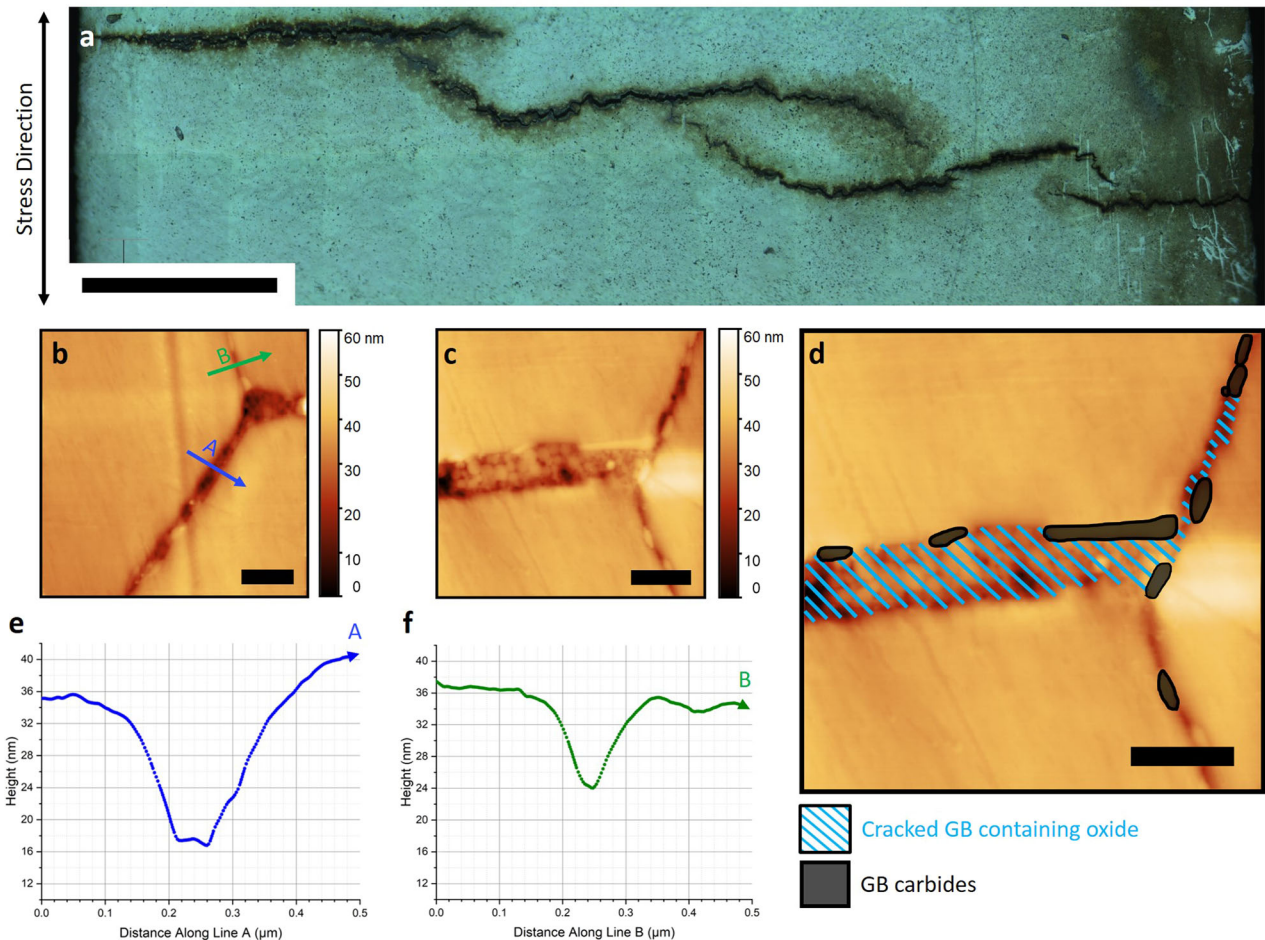


**Fig. 4** Ex situ optical and HS-AFM measurements of IGSCC. **a** An optical image across the whole width of the sample after failure by IGSCC, (scale bar: 500  $\mu\text{m}$ ). **(b)** and **(c)** are images showing HS-AFM topographic maps of a microcrack measured in a different polished cracked sample, with height colour map, imaged within deionised water (scale bars: 500 nm). A labelled version of the image shown in **(c)** is given in **(d)**. Also shown are line profiles collected for: **e** the line labelled A shown in **(b)** as a dark blue line, **f** the line labelled B shown in **(b)** as a green line, showing the difference between cracked GBs and non-cracked GBs. Height measurements have an error of  $\pm 15$  pm.

an uplift of the GBs above the subsurface crack tip, as a result of displacement.

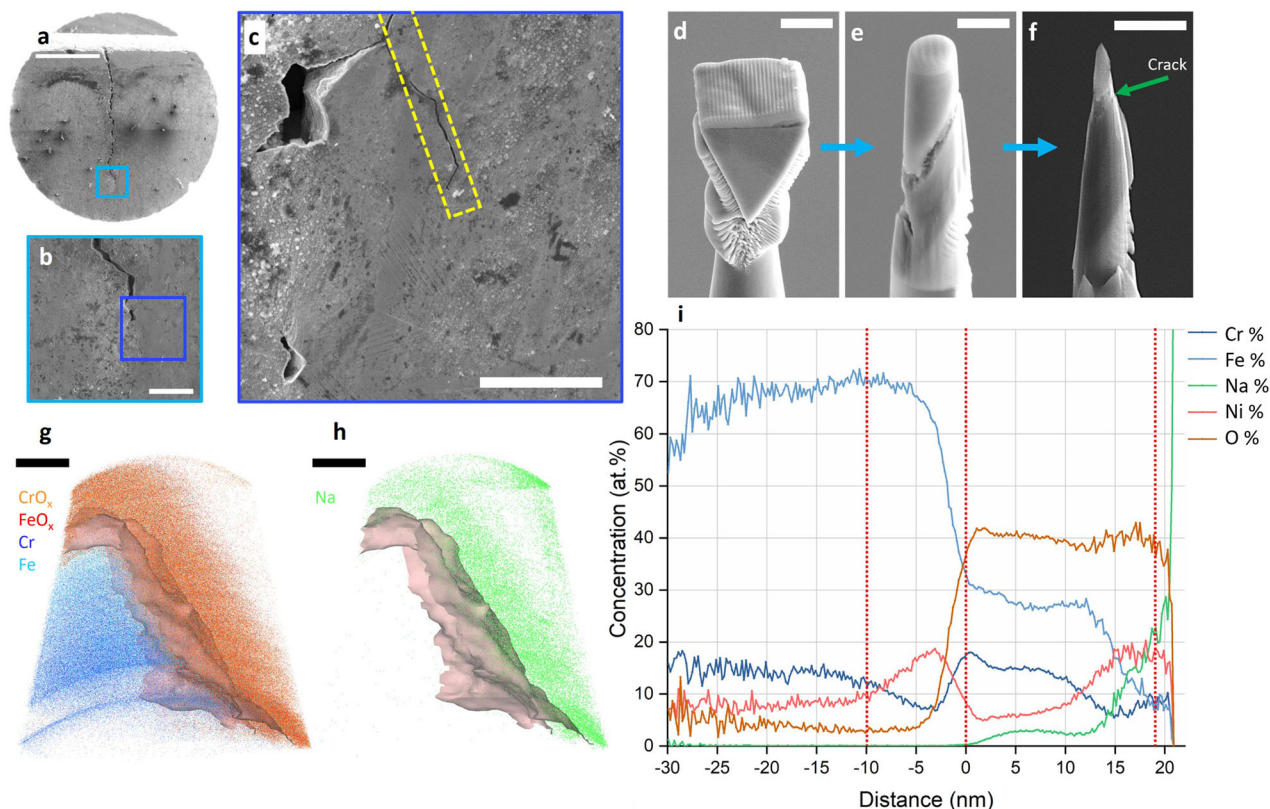
Subsequent to measurements of GB uplift, in situ observation of IGSCC crack propagation by HS-AFM was successfully performed, allowing for measurements of crack growth, shown in Fig. 3e–h. These data were collected approximately 1 h 35 min after the onset of cracking. The tip of the crack is observed at the top of the frame in Fig. 3e, leading down into a GB. This is contrary to optical images of crack propagation (Supplementary Fig. 5), where the crack is progressing upwards. This indicates that the crack had propagated upwards below the surface, before appearing to crack downwards in the HS-AFM image, this further highlights the apparent prominence of subsurface effects previously indicated by measurements of uplift. The GB in Fig. 3e also appears uplifted with respect to the bulk.

Figure 3f shows the progression of the crack 97 s after Fig. 3e. The images collected reveal a highly deformed region at the tip of the crack. The large height range and increased presence of corrosion product results in inevitable loss of resolution making the data somewhat difficult to interpret. Despite this, crack propagation is evident as the crack has grown in length and width. Comparing Fig. 3e and Fig. 3f, the crack is observed to propagate downwards through the frame at approximately  $23 \text{ nm s}^{-1}$ . The crack velocity observed here is orders of magnitude slower than the  $8 \mu\text{m s}^{-1}$  observed in other studies<sup>22</sup>. However, the value given here is calculated from two consecutive images

and so may not be representative of the system. Figure 3g shows the crack 210 s after Fig. 3e has extended across the whole frame. As the cracking progresses further in Fig. 3h, a steady increase in width is observed.

IGSCC was observed to occur as a smooth, continuous process rather than a stepwise process. This contrasts with previous studies where cracks were found to grow as discrete microcracks, considered to be indicative of a hydrogen fracture mechanism<sup>24,25</sup>. However, it must be noted that the observations were performed at the surface, and it is possible that any subsurface cracking progressed in a stepwise fashion. The deformed region at the crack tip may contain strain-induced martensite, as measured in other works<sup>40</sup>; however, in this study this behaviour was not clearly observed.

As the crack becomes wider and deeper, the resultant topographic maps begin to exhibit imaging artefacts due to the nature of AFM. In particular, as the crack deepens, the measurement is affected by tip convolution. For this reason, HS-AFM is most suited for the dynamic in situ measurement of crack initiation and the very early stages of SCC, rather than the later stages. These are the stages that other techniques struggle to image due to environmental requirements and both spatial and temporal resolution limitations. By combining the strengths of multiple techniques, a more complete picture of the SCC process can be achieved.



**Fig. 5** Ex situ APT measurements of IGSCC. Secondary electron images showing: (a) An arrested crack in a sample following failure by IGSCC (scale bar: 500  $\mu\text{m}$ ), (b) a higher magnification image of the region outlined in light blue in (a) (scale bar: 50  $\mu\text{m}$ ), (c) a higher magnification image of the region outlined in dark blue in (b) with the region of APT analysis outlined by a dotted yellow box (scale bar: 20  $\mu\text{m}$ ), (d) a segment of the area outlined in yellow in (c) mounted onto an APT grid (scale bar: 2  $\mu\text{m}$ ), (e) an intermediate needle following FIB thinning (scale bar: 1  $\mu\text{m}$ ), and (f) the final APT needle seen to contain a section of the crack with the crack running diagonally across as indicated (scale bar: 1  $\mu\text{m}$ ). Also shown are 3D APT reconstructions containing a 37 at.% oxygen iso-concentration surface with: (g)  $\text{CrO}_x$ ,  $\text{FeO}_x$ , Cr and Fe ions (scale bar: 10 nm), and (h) (2 $\times$  size) Na ions (scale bar: 10 nm). i Shows a deconvoluted proximity histogram showing the concentration profile either side of the 37 at.% oxygen iso-concentration surface shown in (g) and (h), red dotted lines indicate boundaries between compositionally differing regions. An additional version of (i) with error bars is given in Supplementary Fig. 6.

#### Ex situ analysis of SCC

An optical image of a specimen which had failed by IGSCC in a solution of 395  $\text{mg L}^{-1}$  aqueous sodium thiosulfate is shown in Fig. 4a. This image shows the whole width of a sample and provides an overview of the macroscale cracks. IGSCC was observed to initiate at a number of sites along the apex of the bend, where stress and strain are localised. Cracks were observed to propagate from these initiation points, causing an alteration of the stress state of the sample. These cracks joined to form a crack extending over the width of the sample resulting in the curved crack shape observed. The discolouration that surrounds the crack is likely to be oxidation that originated at the crack tip.

Ex situ HS-AFM topographic maps of cracked GBs are shown in Fig. 4b–d. These images were collected by tracing a deflected crack that branched away from the main crack. Figure 4b, c contains GB triple points in which certain GBs have widened as a result of IGSCC, whereas others remain relatively unchanged, as labelled in Fig. 4d. This is highlighted by comparing the line scans shown in Fig. 4e, f. The line scan collected across the GB that has started to crack is approximately twice the width of the non-cracked GB. By comparing the non-cracked GB line profile in Fig. 4f to that collected from the non-cracked sample in Fig. 2d, it can be seen that GBs are similar in size and shape. This highlights the localised nature of IGSCC. There are a number of parameters that may affect the propensity of a GB to suffer IGSCC. Within this system the degree of sensitisation and local stress are considered to be key factors<sup>23,24,27</sup>.

Carbide precipitates are present within uncracked and cracked GBs (Fig. 4b, c). This indicates that the carbide dissolution observed in Fig. 2b was not prominent during IGSCC. The carbide precipitates in the cracked GB are along one edge of the boundary, indicating that it had parted during IGSCC following the dissolution of the chromium depleted areas adjacent to the carbide precipitates. The asymmetry of dissolution along the crack is likely to arise from the different orientations of the grains either side of the crack, and the relative crystallographic coherence of the carbide precipitate with either grain<sup>40</sup>. This also relates to an asymmetry of the local Cr depletion, resulting in the preferential dissolution of the higher energy carbide–GB interface<sup>40</sup>. An additional factor may be GB migration during thermal sensitisation<sup>40,41</sup>.

The cracked GBs shown in Fig. 4b, c contain an oxide layer, possibly as a result of GB oxidation at, or ahead of, the crack tip. This oxide does not uniformly fill the GB, indicating that it is porous. Chemical analysis of this oxide layer was performed by APT. Samples evaluated by APT were extracted using a site-specific FIB lift-out preparation method adapted from Lotharukpong et al.<sup>42</sup> from a region containing an arrested crack tip, shown in Fig. 5a–f.

Figure 5g shows a 3D APT atom map of the needle selectively showing Cr and Fe ions, as well as  $\text{CrO}_x$  and  $\text{FeO}_x$  ions. The needle contains two distinct regions: a region of oxide, and a region of bulk metal. Within this figure, these two regions are separated by a 37 at.% oxygen iso-concentration surface. Figure 5h shows the

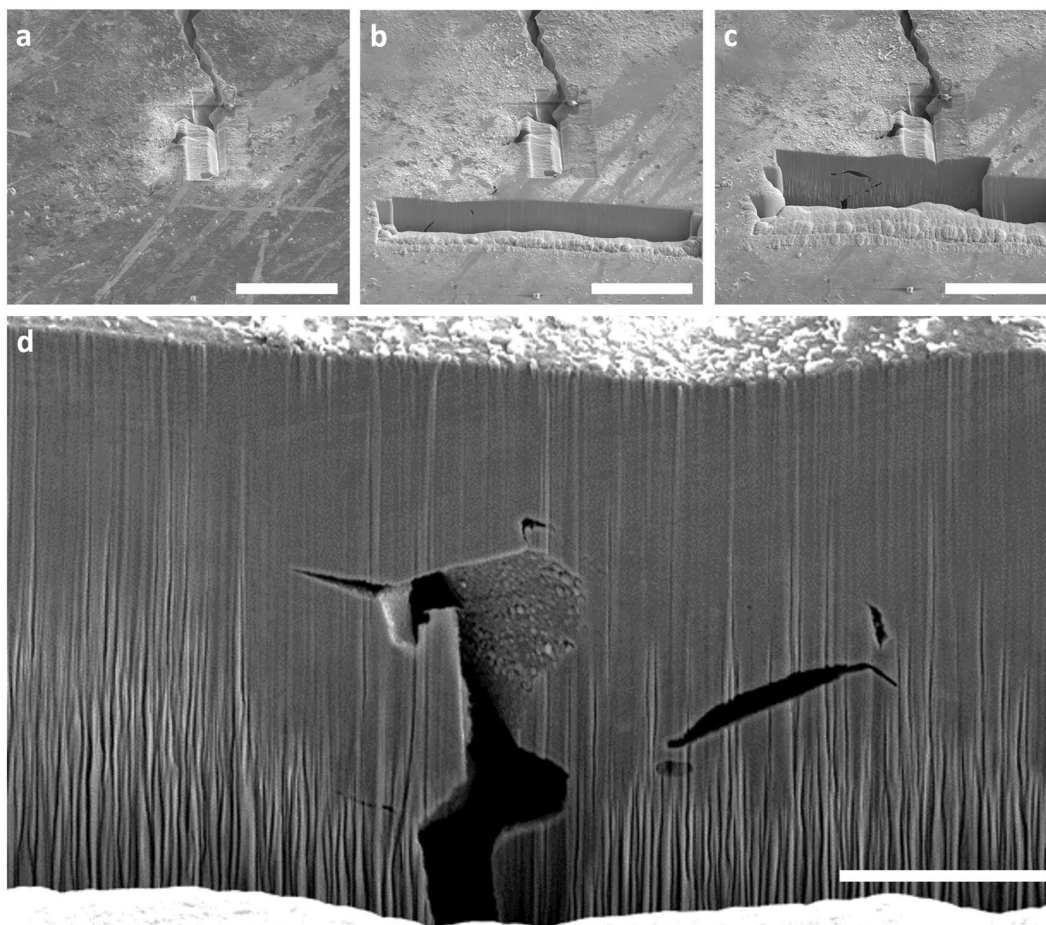


**Fig. 6 Ex situ FIB milling showing subsurface IGSCC.** (a)–(d) show secondary electron images collected as a part of a series of FIB slices into the area ahead of a crack tip, in the same region as that analysed by APT (a–c) scale bars: 50  $\mu\text{m}$ , (d) scale bar: 10  $\mu\text{m}$ ). All images were collected at a tilt of 52° relative to the electron beam. Additional secondary electron images showing intermediate FIB cuts are given in Supplementary Fig. 7.

same needle containing only the oxygen iso-concentration surface and (2 $\times$  size) Na ions. The oxide region of the needle appears to contain a lower density of ions than the metallic region. This is expected to be partly due to the porous structure of the oxide, and partly due to the metal and the oxide having different evaporation fields resulting in trajectory aberrations<sup>43</sup>.

Figure 5i contains a deconvoluted proximity histogram for the 37 at.% oxygen iso-concentration surface showing the variation of relative element concentrations from the bulk metal to the oxide (a version including error bars is shown in Supplementary Fig. 6). The histogram shows variations in Cr, Fe, Na, Ni, and O. Other elements were detected at significantly lower at.% and so have been excluded from this graph. Four distinct sections can be interpreted from this graph: the bulk metal (up to  $-10$  nm), the oxide interface or GB ( $-10$  nm to 0 nm), the oxide (0 nm to 19 nm), and outside the oxide (19 nm onwards). The oxide has a varying composition indicating a layered structure. An inner Cr-rich oxide is indicated by a small peak in Cr up to 18 at.% at 0.5 nm. Notably, the oxide thickness (approximately 20 nm) is comparable to GB uplift observed during in situ IGSCC measurements, Fig. 3a.

Cr is observed to be depleted at the oxide interface, i.e. the GB, down to a value of 6.8 at.%. This corresponds to approximately 7 wt.%, indicating that the GB is severely sensitised. Additionally, there is Ni enrichment up to 18 at.% at the GB, which can occur during thermal sensitisation<sup>41</sup>. In previous works, it has been suggested that sulfur enhances the dissolution of Fe and Ni<sup>22,24,30</sup>,

and since Fe is more electrochemically active than Ni, selective dissolution amplifies Ni enrichment.

Previous works have reported that the accumulation of adsorbed S at the crack tip is an important mechanism for IGSCC for this system. However, APT results for S were not conclusive as it is a challenge to accurately deconvolute the overlap between the S peak from the O<sub>2</sub> peak within the mass spectrum<sup>44</sup>. Notably, 32 Da ions were identified below the apparent surface of the metal which could indicate the presence of adsorbed sulfur or oxygen. Future work will aim to deconvolute these signals; however, this is beyond the scope of the work presented here.

Outside of the oxide the metallic contributions are observed to rapidly reduce towards 0 at.%, and Na concentration increases significantly. This Na likely originated from the retained solution in the porous outer oxide and crack tip post-testing.

Within surface images of the cracked sample, the crack tip was discontinuous, indicating that the crack had propagated subsurface. FIB milling was performed ahead of a crack tip, shown in Fig. 6a, b. These images demonstrated that subsurface GBs ahead of the surface crack tip had indeed been corroded. A series of secondary electron images were collected as the serial sectioning progressed closer to the crack tip on the surface, shown in Fig. 6b–d. These images reveal a network of subsurface intergranular cracks. The porous outer oxide in Fig. 6d is observed along the walls of the corroded GBs, as observed previously by HS-AFM and APT (Figs 4b–d and 5e, f). This was supported by additional EDX measurements (Supplementary Fig. 8). The outer oxide's porous

structure is consistent with a deposited corrosion product and not a passivating oxide observed in some high-temperature systems.

The oxide thickness varied from 10s to 100s of nanometres. Notably, the oxide does not fill the cracked GB. Cracks with a comparatively thin layer of oxide such as these are consistent with the propagation of the crack being stress driven. This suggests a possible mechanism where oxidation occurs ahead of the crack before being ruptured by stress. This is supported by previous HS-AFM measurements shown in Fig. 4b–c, where the oxide was observed to fill the majority of the crack. These images were collected along GBs that branched away from the visible crack, and so may demonstrate a pre-oxidation phenomenon that weakens the GB allowing for a fracture to occur. To the best of author's knowledge this oxide layer has not been reported previously for this SCC system.

In summary, combining dynamic HS-AFM measurements with complementary composition and subsurface analysis by APT, FIB, and electron microscopy has enabled a detailed analysis of the IGSCC processes occurring on a model system across a range of sub-micrometre length-scales. Drawing together the measurements performed within this study suggests that subsurface crack propagation is a key phenomenon within this system, where limited diffusion allows for a build-up of aggressive electrolyte chemistry within the occluded crack interior. An oxide layer with a layered composition was present on the walls of the subsurface cracks. The oxide layer did not fill the cracks suggesting that the SCC process was stress driven. However, within measurements performed closer to the crack tip the oxide was observed to fill the crack, indicating a possible pre-oxidation phenomenon. This was supported by GB uplift observations as the oxide layer occurred on a similar length scale to the observed GB uplift effect, suggesting a possible mechanistic connection. It may be postulated that oxide formation at and ahead of the subsurface crack tip may result in uplift of the GBs at the surface prior to rupture. Furthermore, in situ measurements showed a smooth crack propagation process. Whilst the oxide observations may support a film rupture mechanism similar to that proposed in previous works<sup>22</sup>, inherent contributions from other mechanisms such as hydrogen induced fracture cannot be ruled out. However, it is clear from the measurements performed that the crack growth process is highly localised and combines both chemical and mechanical processes. Whilst the presented study does not explicitly favour a particular model for cracking, some key mechanisms have been observed that are previously unreported, including GB uplift, the role of an oxide layer and the precedence of subsurface crack propagation.

To conclude, high-resolution measurements have provided important insights into the SCC system studied and may be applied to other systems in future. In situ observations of surface crack propagation performed by HS-AFM allows for better understanding of the evolution of the cracking process as it happens, rather than only characterising the failed specimen after cracking has finished. Combining these observations of real-time quantitative morphology evolution with chemical composition and structural information using other cutting-edge techniques such as APT is essential to inform models of SCC and provide evidence for SCC mitigation methodologies.

## METHODS

### Materials and sample preparation

Samples were cut from a 1 mm thick sheet of AISI Type 304 stainless steel supplied by Goodfellow Cambridge Ltd. (Huntingdon, UK) by waterjet. Material composition was measured by inductively coupled plasma optical emission spectrometry (ICP-OES) and combustion by Element Materials Technology (Sheffield, UK), and is given within Table 1. This sheet was thermally sensitised at 600 °C for 70 h within an oven and allowed to air

**Table 1.** Elemental composition of AISI Type 304 stainless steel (weight %).

C	Si	Mn	P	S	Cr	Mo	Ni	Fe
0.059	0.34	1.47	0.022	0.005	18.46	0.08	7.93	Bal.

cool. Samples were cut from this sheet into two different sample geometries: 20 mm × 5 mm rectangles, or 3.5 mm width dog-bone shapes, as shown in Supplementary Fig. 3.

The upper layers of the sample were removed by polishing using sequential coarse (FEPA grit P120) to fine (P4000) grade silicon carbide (SiC) grit paper, with a water lubricant. The surface was then polished using progressively finer (3–0.25 μm) diamond pastes (Kemet International Ltd., KD Diamond Pastes), using a Struers™ DP-Lubricant (Brown). Lastly, the sample was vibropolished (VibroMet™, Buehler) with colloidal silica (MasterMet®, Buehler) for 12 h, producing a mirror finish. Once polished the sample was rinsed thoroughly with water and detergent. The sample was then cleaned by twice placing it into an ultrasonic bath with acetone. This step was repeated with (HPLC-grade) ethanol then isopropanol before rinsing with Milli-Q™ water and drying with lint-free paper to avoid drying marks. This process is described in more detail by Warren et al.<sup>45</sup>

### High-speed atomic force microscopy

The contact-mode HS-AFM (Bristol Nano Dynamics Ltd., UK) produces nanometre resolution topographic maps by monitoring the mechanical response of a cantilever with a sharp probe at its tip as it is raster scanned across the sample surface<sup>13</sup>. A laser beam is scattered from the back of the cantilever and detected by an interferometric detection system, allowing for the z-displacement of the cantilever to be accurately measured to within ±15 pm. This information is used to build topographic images of the surface in real-time using bespoke software (Bristol Nano Dynamics Ltd., UK). These data were further analysed post-collection using Gwyddion SPM data processing software, version 2.53. The HS-AFM is also equipped with a ×20 optical microscope for the identification of features across the surface. Following surface preparation, the sample is secured in a bespoke piezo flexure stage that translates the sample beneath the probe, allowing for specific areas of interest to be imaged.

### SCC tests

Experimental set-up for SCC tests is shown in Supplementary Fig. 3. A micro three-point strain rig was designed such that samples could be imaged under tensile stress, whilst immersed within 395 mg L<sup>-1</sup> aqueous sodium thiosulfate (Na<sub>2</sub>S<sub>2</sub>O<sub>3</sub>). A three-point bend design was chosen as strain is localised and the area of peak stress is small. The time to initiate was found to vary significantly with time exposed to 395 mg L<sup>-1</sup> aqueous sodium thiosulfate before the application of tensile stress. Sample pre-exposure durations were varied between 0 and 20 days. It was found that by pre-exposing the sample to the solution for a duration of 6 days prior to plastically stressing the sample, SCC could be reproducibly initiated within 1 day of the application of stress. Subsequent failure by SCC, defined here as the time for the crack to extend across the width of the sample (3 mm or 5 mm), occurred over the course of a few hours. Thermally sensitised AISI Type 304 stainless steel samples were pre-exposed to 395 mg L<sup>-1</sup> aqueous sodium thiosulfate for 6 days. The sample was then placed onto the strain rig, mounted onto a 12.5 mm SEM pin-stub and secured onto the stage. HS-AFM imaging was performed using a liquid cell with a contact-mode MSNL-10 cantilever (Bruker, USA). Applied load on the specimen could be altered by tightening or loosening the bolts, resulting in a change in the vertical deflection of the specimen<sup>46</sup>. For the purpose of SCC tests, the specimen was stressed sufficiently to cause plastic deformation, this was achieved by deflecting the sample by 1 ± 0.01 mm, as measured with a calliper. The resultant stress is therefore equal to the materials yield stress. The local maximum strain at the apex of the bend in the dog-bone shaped samples was modelled in Autodesk Inventor 2019 to be 0.02.

HS-AFM imaging was also carried out on pre- and post-cracked samples of sensitised AISI Type 304 stainless steel. Cracked samples were removed from the rig, rinsed with Milli-Q™ water, and mounted in a transparent, thermoplastic acrylic (TransOptic™, Buehler™) mount using a hot press (SimpliMet 4000, Buehler™). These samples were then polished to a mirror finish as described previously.



### FIB milling and scanning electron microscopy

FIB milling and SEM imaging were used in tandem for 3D analysis of a volume beneath the sample surface. Within this work an FEI™ Helios NanoLab™ 600 Dual FIB-SEM system (Hillsboro, Oregon, USA) with a gallium ion source was used. FIB cuts were performed at 30 kV and 6.5–20 nA, and secondary electron images were collected at regular intervals using the SEM at 10 kV and 0.34 nA.

### Energy dispersive X-ray spectroscopy and EBSD

EDX and EBSD analysis were performed using a Zeiss Sigma VP FEG-SEM with a coincident EDAX EDX detector and Digiview™ high-speed digital camera. Measurements were collected at 30 kV with an aperture of 120 μm and processed using TEAM V4.1 (EDAX) and OIM™ data collection and analysis software.

### Atom probe tomography

APT needle specimens were produced using the FIB-SEM instrumentation described for FIB and SEM analysis. This instrument is fitted with an MM3A micromanipulator from Kleindiek Nanotechnik GmbH (Reutlingen, Germany). Seven APT needle specimens were produced from a single lift out containing the cracked GB and a region ahead of the crack tip, outlined in yellow in Fig. 5c. A thin line of platinum was deposited by electron beam along the visible crack tip on the surface, which acted as a fiducial marker to position the crack within the final APT needle specimen. Needles were thinned to a tip diameter of approximately 50 nm by an annular milling method adapted from Lotharukpong et al.<sup>42</sup>. The FIB thinning process for one of the APT needle specimens is illustrated in Fig. 5d–f, where Fig. 5f shows the final APT needle analysed.

APT experiments within this work were carried out using a Cameca LEAP 5000 XR. Specimens were run in laser pulsing mode, a laser pulse energy of 50 pJ and a pulse rate of 200 kHz. The specimen was analysed at a temperature of 50 K, and a detection rate of 0.5% was maintained.

### DATA AVAILABILITY

The raw and processed data required to reproduce these findings are available to download from Moore, Stacy (2020), "Observation of Stress Corrosion Cracking of Stainless Steel Using Real-Time In-Situ High-Speed Atomic Force Microscopy and Correlative Techniques", Mendeley Data, V3, doi: 10.17632/h6p8dgd84c.3.

Received: 22 September 2020; Accepted: 19 December 2020;

Published online: 18 January 2021

### REFERENCES

- Raja, V. & Shoji, T. *Stress Corrosion Cracking: Theory and Practice* (Elsevier, 2011).
- Jones, R. *Stress Corrosion Cracking-Material Performance and Evaluation* (ASM International, 2017).
- Fang, B. et al. Review of stress corrosion cracking of pipeline steels in "low" and "high" pH solutions. *J. Mater. Sci.* **38**, 127–132 (2003).
- McCafferty, E. *Introduction to Corrosion Science* (Springer Science & Business Media, 2010).
- Kalderon, D. Steam turbine failure at Hinkley Point 'A'. *Proc. Inst. Mech. Eng.* **186**, 341–377 (1972).
- Stratulat, A., Duff, J. A. & Marrow, T. J. Grain boundary structure and intergranular stress corrosion crack initiation in high temperature water of a thermally sensitised austenitic stainless steel, observed in situ. *Corros. Sci.* **85**, 428–435 (2014).
- Li, J. X., Chu, W. Y., Wang, Y. B. & Qiao, L. J. In situ TEM study of stress corrosion cracking of austenitic stainless steel. *Corros. Sci.* **45**, 1355–1365 (2003).
- Meisnar, M., Moody, M. & Lozano-Perez, S. Atom probe tomography of stress corrosion crack tips in SUS316 stainless steels. *Corros. Sci.* **98**, 661–671 (2015).
- Badwe, N. et al. Decoupling the role of stress and corrosion in the intergranular cracking of noble-metal alloys. *Nat. Mater.* **17**, 887–893 (2018).
- Uchida, H., Yamashita, M., Inoue, S. & Koterazawa, K. In-situ observations of crack nucleation and growth during stress corrosion by scanning vibrating electrode technique. *Mater. Sci. Eng. A* **319**, 496–500 (2001).
- Clark, R. N. et al. Nanometre to micrometre length-scale techniques for characterising environmentally-assisted cracking: an appraisal. *Heliyon* **6**, e03448 (2020).

- Binnig, G., Quate, C. F. & Gerber, C. Atomic force microscope. *Phys. Rev. Lett.* **56**, 930 (1986).
- Payton, O. D., Picco, L. & Scott, T. B. High-speed atomic force microscopy for materials science. *Int. Mater. Rev.* **61**, 473–494 (2016).
- Minoshima, K., Oie, Y. & Komai, K. In situ AFM imaging system for the environmentally induced damage under dynamic loads in a controlled environment. *ISIJ Int.* **43**, 579–588 (2003).
- Nakai, Y., Kusukawa, T. & Hayashi, N. Grain-size effect on fatigue crack initiation condition observed by using atomic-force microscopy. *ASTM STP* **1406**, 122–135 (2001).
- Komai, K., Minoshima, K. & Miyawaki, T. In situ observation of stress corrosion cracking of high-strength aluminum alloy by scanning atomic force microscopy and influence of vacuum. *JSME Int. J. A-Solid Mech. Mater. Eng.* **41**, 49–56 (1998).
- Payton, O. D. et al. High-speed atomic force microscopy in slow motion—understanding cantilever behaviour at high scan velocities. *Nanotechnology* **23**, 205704 (2012).
- Cullen, P. L. et al. Ionic solutions of two-dimensional materials. *Nat. Chem.* **9**, 244–249 (2017).
- LaFerrere, A. et al. In situ imaging of corrosion processes in nuclear fuel cladding. *Corros. Eng. Sci. Technol.* **52**, 596–604 (2017).
- Moore, S. et al. A study of dynamic nanoscale corrosion initiation events using HS-AFM. *Faraday Discuss.* **210**, 409–428 (2018).
- Pyne, A. et al. High-speed atomic force microscopy of dental enamel dissolution in citric acid. *Arch. Histol. Cytol.* **72**, 209–215 (2009).
- Newman, R. C., Sieradzki, K. & Isaacs, H. S. Stress-corrosion cracking of sensitized type 304 stainless steel in thiosulfate solutions. *Metall. Trans. A* **13**, 2015–2026 (1982).
- Isaacs, H. S. Initiation of stress corrosion cracking of sensitized type 304 stainless steel in dilute thiosulfate solution. *J. Electrochem. Soc.* **135**, 2180 (1988).
- Wells, D. B., Stewart, J., Davidson, R., Scott, P. M. & Williams, D. E. The mechanism of intergranular stress corrosion cracking of sensitised austenitic stainless steel in dilute thiosulphate solution. *Corros. Sci.* **33**, 39–71 (1992).
- Gomez-Duran, M. & Macdonald, D. D. Stress corrosion cracking of sensitized Type 304 stainless steel in thiosulfate solution: I. Fate of the coupling current. *Corros. Sci.* **45**, 1455–1471 (2003).
- Gomez-Duran, M. & Macdonald, D. D. Stress corrosion cracking of sensitized Type 304 stainless steel in thiosulphate solution: II. Dynamics of fracture. *Corros. Sci.* **48**, 1608–1622 (2006).
- Roychowdhury, S., Ghosal, S. K. & De, P. K. Role of environmental variables on the stress corrosion cracking of sensitized AISI type 304 stainless steel (SS304) in thiosulfate solutions. *J. Mater. Eng. Perform.* **13**, 575–582 (2004).
- Sato, Y., Atsumi, T. & Shoji, T. Continuous monitoring of back wall stress corrosion cracking growth in sensitized type 304 stainless steel weldment by means of potential drop techniques. *Int. J. Press. Vessel.* **84**, 274–283 (2007).
- Kovac, J., Alaux, C., Marrow, T. J., Govekar, E. & Legat, A. Correlations of electrochemical noise, acoustic emission and complementary monitoring techniques during intergranular stress-corrosion cracking of austenitic stainless steel. *Corros. Sci.* **52**, 2015–2025 (2010).
- Choudhary, L., Macdonald, D. D. & Alfantazi, A. Role of thiosulfate in the corrosion of steels: a review. *Corrosion* **71**, 1147–1168 (2015).
- Choudhary, L., Wang, W. & Alfantazi, A. Electrochemical corrosion of stainless steel in thiosulfate solutions relevant to gold leaching. *Metall. Mater. Trans. A* **47**, 314–325 (2016).
- Zhao, R., Xia, D.-H., Song, S.-Z. & Hu, W. Detection of SCC on 304 stainless steel in neutral thiosulfate solutions using electrochemical noise based on chaos theory. *Anti-Corros. Method M.* **64**, 241–251 (2017).
- Whillock, G. O., Hands, B. J., Majchrowski, T. P. & Hambley, D. I. Investigation of thermally sensitised stainless steels as analogues for spent AGR fuel cladding to test a corrosion inhibitor for intergranular stress corrosion cracking. *J. Nucl. Mater.* **498**, 187–198 (2018).
- Yanliang, H., Kinsella, B. & Becker, T. Sensitisation identification of stainless steel to intergranular stress corrosion cracking by atomic force microscopy. *Mater. Lett.* **62**, 1863–1866 (2008).
- Martin, F., Cousty, J., Masson, J. & Bataillon, B. In situ AFM study of pitting corrosion and corrosion under strain on a 304L stainless steel. *Congr. Proc. EURO-CORR* **16**, 1–10 (2004).
- Payam, A. F. et al. Development of fatigue testing system for in-situ observation of stainless steel 316 by HS-AFM & SEM. *Int. J. Fatigue* **127**, 1–9 (2019).
- Fréchalard, S., Martin, F., Clément, C. & Cousty, J. AFM and EBSD combined studies of plastic deformation in a duplex stainless steel. *Mater. Sci. Eng.: A* **418**, 312–319 (2006).
- Li, L., Liu, S., Ye, B., Hu, S. & Zhou, Z. Quantitative analysis of strength and plasticity of a 304 stainless steel based on the stress-strain curve. *Met. Mater. Int.* **22**, 391–396 (2016).

39. Burt, D. P., Wilson, N. R., Janus, U., Macpherson, J. V. & Unwin, P. R. In-situ atomic force microscopy (AFM) imaging: influence of AFM probe geometry on diffusion to microscopic surfaces. *Langmuir* **24**, 12867–12876 (2008).
40. Butler, E. P. & Burke, M. G. Chromium depletion and martensite formation at grain boundaries in sensitised austenitic stainless steel. *Acta Metall.* **34**, 557–570 (1986).
41. Ortner, S. R. A STEM study of the effect of precipitation on grain boundary chemistry in AISI 304 steel. *Acta Metall. Mater.* **39**, 341–350 (1991).
42. Lotharukpong, C. et al. Specimen preparation methods for elemental characterisation of grain boundaries and isolated dislocations in multicrystalline silicon using atom probe tomography. *Mater. Charact.* **131**, 472–479 (2017).
43. Gault, B., Moody, M. P., Cairney, J. M. & Ringer, S. P. *Atom Probe Microscopy* Vol. 160 (Springer Science & Business Media, 2012).
44. Meiners, T., Peng, Z., Gault, B., Liebscher, C. H. & Dehm, G. Sulfur-induced embrittlement in high-purity, polycrystalline copper. *Acta Mater.* **156**, 64–75 (2018).
45. Warren, A. D., Martinez-Ubeda, A. I., Payton, O. D., Picco, L. & Scott, T. B. Preparation of stainless steel surfaces for scanning probe microscopy. *Microsc. Today* **24**, 52–55 (2016).
46. Davis, J. R. *Corrosion of Aluminum and Aluminum Alloys* 2nd edn (ASM International, 1999).

## ACKNOWLEDGEMENTS

The authors would like to thank Dr. Scott Greenwell for providing an optical stitch of the sample, the physics workshop and the NSQI low noise labs at the University of Bristol. The PhD studentship for S.M. was funded by the National Nuclear Laboratory (NNL) and the Engineering and Physical Sciences Research Council (EPSRC). O.P. was supported by a fellowship awarded by the Royal Academy of Engineering (RAEng). EPSRC funding for the LEAP 5000XR atom probe for the UK National Atom Probe Facility was provided under the grant number EP/M022803/1.

## AUTHOR CONTRIBUTIONS

S.M. prepared bulk samples, performed HS-AFM characterisation, SCC tests, and analysed the resultant data, and participated in APT sample preparation/characterisation and subsurface FIB/SEM characterisation. R.B. performed SCC tests, and assisted in experimental design and interpretation of the data. D.K. and M.B.K. performed SCC tests and measurements of strain induced by the three-point strain rig. A.D.W. assisted in EBSD characterisation and in the interpretation of the data. P.E. J.F. assisted in interpretation of the data. L.P. and O.D.P. assisted in HS-AFM

characterisation, experimental design, and developed the HS-AFM facility at the University of Bristol. T.L.M. led APT sample preparation/characterisation, subsurface FIB/SEM characterisation, and assisted in experimental design and interpretation of the data. S.M. wrote this manuscript. R.B., A.D.W., P.E.J.F., L.P., O.D.P. and T.L.M. all contributed to the editing of this manuscript.

## COMPETING INTERESTS

O.D.P. and L.P. are shareholders in Bristol Nano Dynamics Ltd., a University of Bristol spin-out company.

## ADDITIONAL INFORMATION

**Supplementary information** is available for this paper at <https://doi.org/10.1038/s41529-020-00149-y>.

**Correspondence** and requests for materials should be addressed to S.M.

**Reprints and permission information** is available at <http://www.nature.com/reprints>

**Publisher's note** Springer Nature remains neutral with regard to jurisdictional claims in published maps and institutional affiliations.



**Open Access** This article is licensed under a Creative Commons Attribution 4.0 International License, which permits use, sharing, adaptation, distribution and reproduction in any medium or format, as long as you give appropriate credit to the original author(s) and the source, provide a link to the Creative Commons license, and indicate if changes were made. The images or other third party material in this article are included in the article's Creative Commons license, unless indicated otherwise in a credit line to the material. If material is not included in the article's Creative Commons license and your intended use is not permitted by statutory regulation or exceeds the permitted use, you will need to obtain permission directly from the copyright holder. To view a copy of this license, visit <http://creativecommons.org/licenses/by/4.0/>.

© The Author(s) 2021